Electronic Journal of Structural Engineering

Original Article

Cite this: DOI:10.56748/ejse.26875

Received Date:3 September 2025
Accepted Date: 23 February 2026

1443-9255
https://ejsei.com/ejse

Seismic behavior of five-story coupled steel plate reinforced concrete composite walls

Yongchang Li [a], Yuntian Wu [b*], Hao Huang [b]

[a] School of Civil Engineering, Chongqing University, Chongqing 400044, China
[b] Department of Civil and Environmental Engineering, University of Idaho, Moscow, ID 83844, USA
*Corresponding author: yuntianw@uidaho.edu

Abstract

Due to the lack of research background, steel plate reinforced concrete (SPRC) wall piers constructed in the core tubes of super tall buildings in seismic regions have been designed as isolated SPRC walls without considering their interaction (coupling action) provided by the steel link (coupling) beams at floor levels, which may lead to poor material efficiency and underestimated overall performance. Research is urgently needed to examine the seismic performance of multi-pier SPRC walls joined by steel coupling beams at floor levels and provide design suggestions if coupling action is considered. In this research program, a 1/4-scaled two-pier and five-story coupled SPRC wall test model with a coupling ratio of 0.3 was constructed and tested under reversed cyclic lateral loading and constant axial compression. Test results showed stable lateral force versus displacement hysteretic behavior with adequate post-yield deformation ductility, great energy dissipation, and strength retention capacities. The coupling mechanism between SPRC walls and steel coupling beams ensured the expected plasticity and damage distribution pattern. The concrete cracking was insignificant along the entire height of the SPRC wall piers. Steel coupling beams of all floor levels developed considerable inelastic shear deformation and consumed most of the input energy. A numerical simulation of the test model was conducted, and its accuracy was verified against the main experimental results. Parametric analyses were conducted to further investigate the effects of key design parameters on the overall structural response of the coupled SPRC walls. The results indicate that increasing the axial load ratio and steel plate ratio or decreasing the flexure-to-shear ratio of the steel coupling beam can enhance the lateral load carrying capacity. The medium value of 0.15 for axial load ratio, a medium value of 6.6% for steel plate ratio, and a shear-to-flexure ratio of 1.0 for steel coupling beams can result in the best displacement ductility.

Keywords

Coupled wall, Structural wall, Steel coupling beam, Seismic behavior, Finite element analysis, Parametric analysis

1. Introduction

Steel plate shear walls (SPSW) and reinforced concrete (RC) shear walls have been widely constructed as the lateral-force resistance systems for tall buildings in seismic regions, respectively (ACI 318-2014; AISC 361-2016). When the structural height further increases up to hundreds of meters, the lower portion of such a super tall building will be subjected to extremely high axial loads, causing structural and construction problems such as high axial load ratio, large wall thickness, and an excessive amount of reinforcement. To achieve material efficiency and enhanced constructability, the steel plate reinforced concrete (SPRC) wall has become a popular alternative to RC wall or SPSW for use in super tall buildings (Zhang et al. 2021). By embedding steel plates into RC wall and ensuring their effective interaction through shear studs, the SPRC section can exhibit much greater load carrying, deformation and energy dissipation capacities than a RC wall with similar thickness. It will also provide fire resistance, stability, dynamic properties, and durability superior to the SPSW (Dey et al. 2016; Nguyen et al. 2017; Wang et al. 2017; Wang et al. 2019). Current building codes have provided guidance on the design of SPRC walls (AISC 361-2016; JGJ138-2016). The calculation methods for axial, shear and bending moment capacities of the SPRC cross section are available. Another type of steel plate and concrete composite wall is the composite plate shear walls/concrete filled (C-PSW/CF), where two steel web plates and two flange plates define a hollow box section that is filled with concrete (Varma et al. 2019; Shafaei et al. 2021; Kizilarslan et al. 2023).

For isolated SPRC walls, although the load carrying capacities are significantly enhanced, their failure patterns remain the same as the conventional RC walls, i.e., damages locally concentrated at bottom regions. In real-world construction, however, SPRC walls rarely exist in an isolated fashion. To support and provide space for elevators, two or more SPRC walls are placed adjacently surrounding the core tube and joined by steel link beams at all floor levels, forming the coupled SPRC walls. According to statistical data, such coupled SPRC walls have been used in most of the super tall buildings with structural heights over 400 meters or those with height over 200 meters in high seismic regions in mainland China. It is noted that the SPRC walls are only needed for the bottom stories and basement to satisfy the stringent seismic design requirements. The construction of a coupled SPRC wall is shown in Fig. 1. Due to the lack of research background, the SPRC walls of the coupled SPRC wall system are designed as isolated SPRC walls following current code specifications. However, if the coupling action provided by the steel coupling beams is considered, the coupled SPRC walls can be designed in a much more efficient manner.

The earthquake-induced responses of a coupled SPRC wall system are substantially different from the sum of its component SPRC wall piers (Abdelatee et al. 2014). Previous research has revealed many advantages of coupled wall systems thanks to the coupling action (El-Tawil et al. 2010; Bengar et al. 2016; Gorji et al. 2018; Oh et al. 2019; Das et al. 2020). The shear forces transferred from the coupling beams to the wall piers can form tension-compression force couples between adjacent walls, which contribute a great deal to the overturning moment resistance. The ratio of this tension-compression force couple corresponding to full yielding of the steel coupling beams in shear to the total earthquake-induced overturning moment is called the coupling ratio (CR), which is used to measure the contribution of the coupling action to the overturning moment resistance of the coupled system. coupling beams can be designed to consume most of the inelastic energy through post-yield plastic deformations and distribute damages along the entire wall height. In addition, bottom regions of the wall piers can be well protected from excessive bending moment demand and damage concentrations. Recent research on coupled walls has focused on the coupled C-PSW/CF, consisting of two C-PSW/CFs linked together by concrete filled tubular (CFT) coupling beams at floor levels. The capacity-based seismic design method was developed to ensure the strong wall-weak coupling beam principle (Kizilarslan et al. 2021). The seismic performance factors and coefficients defined in ASCE 7-2016 for the coupled C-PSW/CF were also studied and suggested. However, research on coupled SPRC walls has rarely been reported largely due to the fact that current codes do not differentiate between coupled and non-coupled SPRC walls (Broberg et al. 2022). Experimental and numerical studies are necessary to reveal the seismic behavior of the coupled SPRC walls and find a solid basis for future codification.

Coupled SPRC walls have been widely constructed in the core tubes of super tall buildings in seismic regions. However, due to the lack of research background and design guidelines in current building codes, SPRC walls have been designed as isolated (individual) walls without considering their interaction (coupling action), which leads to poor material efficiency and underestimated overall seismic performance. To address this research gap and provide research background for future codification of the coupled SPRC wall system, experimental and numerical

research is urgently needed. Compared with the coupled C-PSW/CF, the coupled SPRC walls have better constructability, cost-effectiveness, and are more suitable to super tall building structures. The coupled C-PSW/CF is usually used for special construction such as nuclear facilities. In this research program, a 1/4-scaled five-story and two-pier coupled SPRC wall model with a 30% coupling ratio was constructed and tested to examine the seismic performance in terms of hysteretic responses, stiffness and strength degradation characteristics, energy dissipation, shear deformation of the steel coupling beam and failure pattern. Finite element analysis was then conducted to simulate the overall behavior of the test model. The simulation and experimental results were compared to verify the accuracy and efficiency of the numerical techniques. Parametric analyses were further performed to investigate the influences of such design parameters as axial load ratio, sectional steel ratio, and flexure-to-shear ratio of steel coupling beams on the structural performance of the coupled SPRC wall system.

Fig. 1 Coupled SPRC wall system under construction

2. Experimental program

2.1 Details of test model

The 1/4-scaled five-story and two-pier coupled SPRC wall test model was designed and fabricated in accordance with the relevant Codes (AISC 361-2016; ACI 318-2019). Deviating from the current practice, the SPRC walls of the test model were designed as the coupled wall piers joined by steel coupling beams (SCB). The coupling action provided by the SCBS can be evaluated by the coupling ratio (CR), which is defined as the ratio of the overturning moment resistance provided by the coupling action to that of the entire coupled wall system. In the design of the test model, the plastic CR was adopted to reflect the preferred plasticity development and distribution mode where all the steel coupling beams yield in shear and the bottom regions of the SPRC walls form plastic hinges. Based on previous studies on different coupled wall systems (Borello et al. 2011; Cheng et al. 2015) and the limitation of the test setup, a CR value of 0.3 was chosen as the design CR for the test model. The steel coupling beams were designed to yield significantly and consume considerable amount of inelastic energy by developing adequate plastic shear rotation. Then the SPRC wall piers will continue to provide the required deformation and energy dissipation capacities after the SCBs have reached their post-yield deformation capacity.

The embedded SPSW of the test model is depicted in Fig. 2(a). The overall dimensions of the test model are shown in Fig. 2(b). The width, thickness and story height of the wall pier were 800, 120 and 800 mm, respectively. The clear span of steel coupling beams was 300 mm. H90×60×10×6 steel sections were used for vertical and horizontal boundary elements (VBE and HBE) of the embedded SPSW, as shown in Fig. 2(c). The web plates of the SPSW had a thickness of 6 mm. H150×60×10×4 and H120×60×10×4 shape steel sections were used for the steel coupling beams of the second and third floors [Fig. 2(d)] and the fourth to roof levels [Fig. 2(e)], respectively. The steel coupling beams (SCB) were proportioned so that shear yielding would dominate the inelastic responses. Web stiffener plates were provided to satisfy the requirements of current code (AISC 341-2016). No.6 (6 mm nominal diameter) rebars were used as the uniformly distributed horizontal and vertical wall reinforcements at a spacing of 100 mm. Six No.8 longitudinal rebars were placed at boundary elements of wall piers with No. 8 closed hoops at a spacing of 100 mm as the transverse reinforcement. Headed shear studs with a diameter of 10 mm and spacing of 90 mm were welded on both sides of the web plates and flanges of the vertical boundary elements of the SPSW. Fig. 2 (f) shows the cross-section view of the test model.

2.2 Test setup and loading protocol

The quasi-static cyclic loading test setup is depicted in Fig. 3. For each wall pier the vertical compression corresponding to an axial load ratio of 0.1 was applied by a vertical hydraulic jack with a maximum loading capacity of 1500 kN. A roller track was installed between the vertical jack and the reaction girder so that during testing the hydraulic jack can slide horizontally and remain vertical. A spreader beam was placed on top of each wall pier to distribute the axial load uniformly across the wall section. The reversed cyclic lateral loading was applied by the horizontal actuator with a maximum loading capacity of 1000 kN and a stroke of ±100 mm. Before the commencement of horizontal loading, the axial load was applied to the test model and approximately maintained constant during the entire testing procedure. To avoid overturning, the foundation of the test model was fastened to the strong floor using two rigid beams and high strength steel rods. To prevent horizontal sliding of the test model, hydraulic jacks were placed on both sides of the foundation. The out-of-plane deformation of the test model was restrained by a pair of horizontal rigid steel beams arranged at the 5th floor level. Teflon pads were inserted between the wall surface and the horizontal beams to minimize friction and allow smooth horizontal movement of the wall piers.

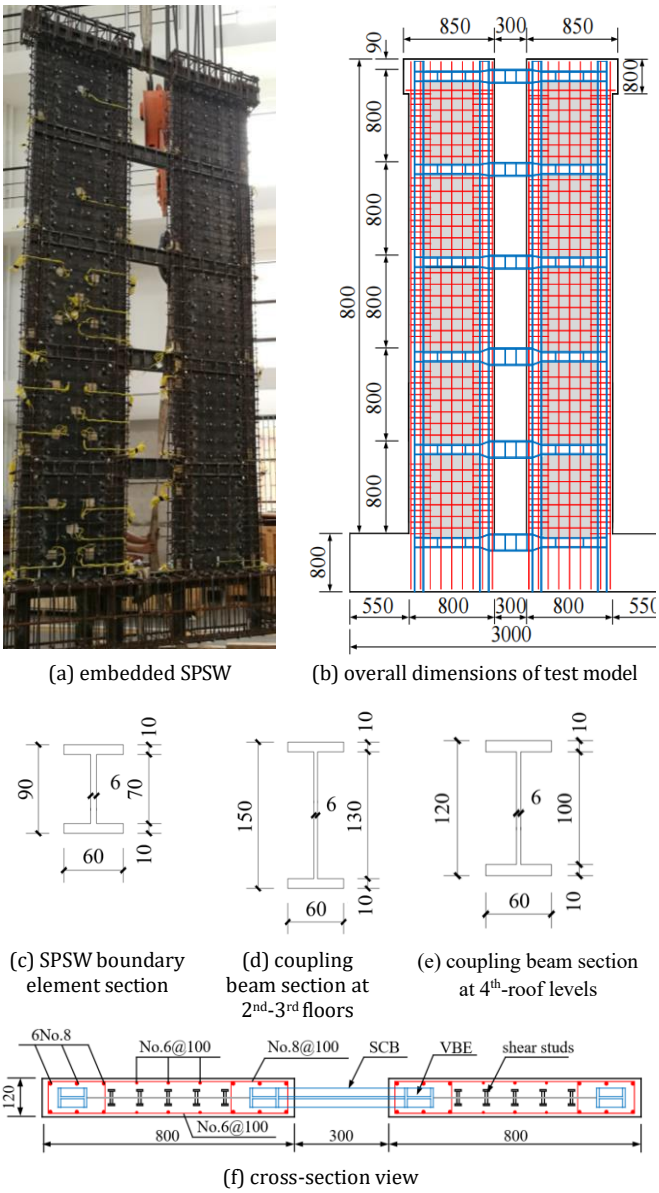

(a) embedded SPSW (b) overall dimensions of test model

(c) SPSW boundary element section (d) coupling beam section at 2nd-3rd floors (e) coupling beam section at 4th-roof levels

(f) cross-section view

Fig. 2 Details and dimensions of test model (unit: mm)

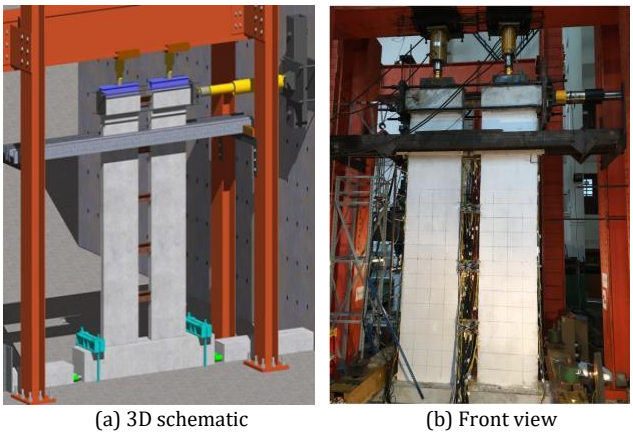

(a) 3D schematic (b) Front view

Fig. 3 Test setup

The displacement-controlled loading history (FEMA 461 2007) was adopted, which consists of repeated cycles of stepwise increasing

deformation amplitudes. Two cycles at each amplitude were completed. The roof lateral drift ratio δ was chosen as the deformation index, which is defined as the ratio of the applied lateral drift at roof level (Δ) to the total structural height of test model (H) measured from the centerline of the horizontal actuator to the top surface of the foundation. The pushing and pulling of the actuator were designated as positive and negative loading directions, respectively. Fig. 4 shows the sequence of the roof lateral drift ratio amplitudes. The test was terminated when the lateral strength of the test model decreased to 85% of the peak lateral load.

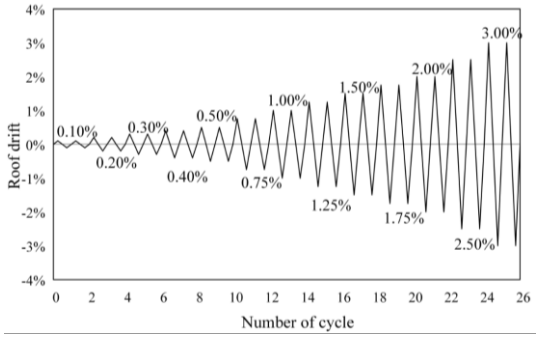

Fig. 4 Loading protocol

2.3 Instrumentation

Five linear variable displacement transducers (LVDTs) with a stroke of ±150 mm were horizontally attached to each floor level of the test model to measure the applied lateral displacements. The shear deformation of steel coupling beams was measured with linear potentiometers with a stroke of ±10 mm mounted on the web plate. Strain gauges were attached to critical locations on steel coupling beams, longitudinal rebars, and the SPSW (Fig. 5).

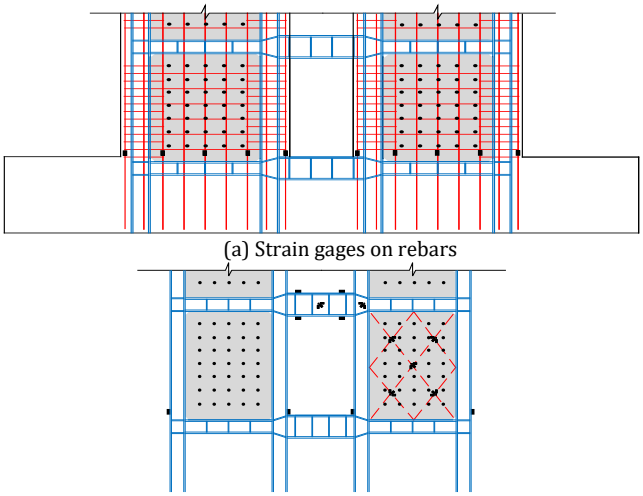

(a) Strain gages on rebars

(b) Strain gages on steel members

Fig. 5 Strain gages arrangement

2.4 Material properties

Mechanical properties of concrete, reinforcement and steel members of the test model were obtained according to relevant Chinese standards (GB/T228-2010; GB/T50081-2019). The average compressive strength of 150×150×150 mm standard cubic concrete samples measured on the 28th curing day were 58.1, 46.4 and 41.5 MPa for the foundation, loading beam and wall pier, respectively. The measured mechanical properties of the rebars and steel shapes are listed in Table 1.

Table 1. Material properties of steel

Steel type	E_s (N/mm²)	f_y (N/mm²)	f_u (N/mm²)
4 mm plate	2.09×10^5	445	520
6 mm plate	2.09×10^5	430	548
8 mm plate	2.07×10^5	433	559
10 mm plate	2.06×10^5	435	565
No.6 rebar	2.06×10^5	543	604
No.8 rebar	2.01×10^5	535	676

3. Experimental Results and Discussion

3.1 Damage development and failure mode

When the roof lateral drift ratio δ was 0.1% (Δ=4mm), horizontal cracks occurred at boundary regions of the first and second stories of wall piers [Fig. 6(a)]. Along with the increase of the roof lateral drift ratio up to 0.4%, these early cracks gradually extended toward the web regions. New cracks also developed at the upper stories [Fig. 6(b)]. Then the cracks uniformly distributed along the wall height remained virtually unchanged without noticeable further development until the failure of the test model [Fig. 6(c)], indicating that the plasticity development of the test model has shifted from wall piers to other elements.

The initiation of the concrete crushing was observed at the bottom of the exterior boundary elements of wall piers corresponding to the roof lateral drift ratio of 1.25% (Fig. 7). Considerable shear deformation has been developed in steel coupling beams in excess of yield strain. The longitudinal rebars at the bottom section of the exterior boundary elements of wall piers have yielded. Along with the further increase of applied roof lateral drift, the concrete crushing became more and more severe and started to spall off when the roof lateral drift ratio arrived at 2.5% (Fig. 8). At the roof lateral drift ratio of 3%, the ultimate failure of the test model was initiated by the cracking of stiffener weld and the fracture of web plate on steel coupling beams at the fourth and fifth floor levels, as shown in Figs. 9-10. At the ultimate failure of the test model, the flanges of the exterior vertical boundary element of SPSW buckled, and the longitudinal rebars on the exterior sides of the wall boundary regions fractured. It is noted that the concrete at the bottom of the interior sides of the boundary elements of the wall piers remained in good shape even as the test model failed.

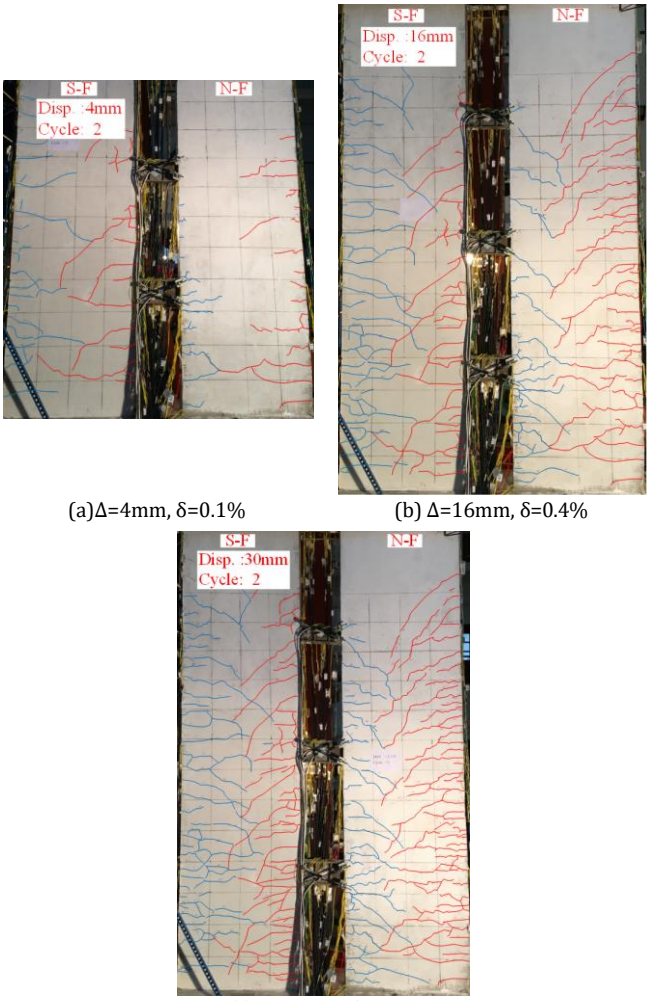

(a)Δ=4mm, δ=0.1%

(b) Δ=16mm, δ=0.4%

(c) Δ=30mm, δ=0.8%

Fig. 6 Cracking development of wall piers

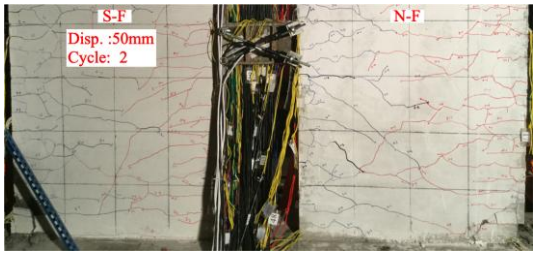

Fig. 7 Initiation of concrete crushing of wall piers (Δ=50mm, δ=1.25%)

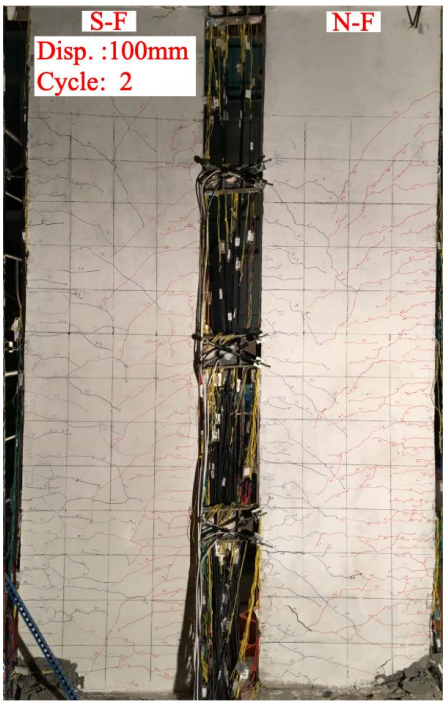

Fig. 8 Spalling off of wall pier concrete (Δ=100mm, δ=2.5%)

Fig. 9 shear failure of steel coupling beam at 4th floor

Fig. 10 shear failure of steel coupling beam on the 5th floor

3.2 Shear rotation angle of steel coupling beam

As shown in Fig. 11, the shear deformation of steel coupling beams can be evaluated by the shear rotation angle γ, which can be estimated as follows:

$$\gamma = \frac{1}{2}(a_1 + a_2 + a_3 + a_4)\frac{\sqrt{a^2+b^2}}{ab} \quad (1)$$

where a_1, a_2, a_3 and a_4 are the elongation and shortening of diagonal lines of the shear deformation region; a_1 and a_2 take positive values in terms of elongation while a_3 and a_4 are positive in the case of shortening; a and b are side lengths of the measured region.

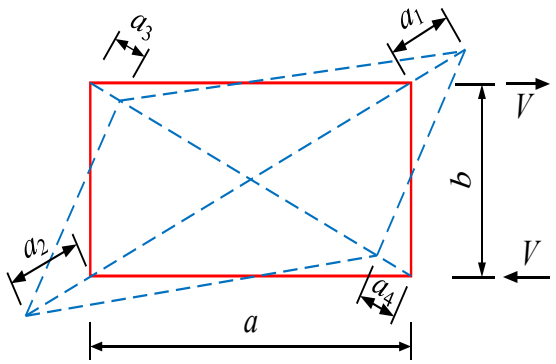

Fig. 11 Diagram of shear rotation angle calculation

Fig. 12 shows the variation of shear rotation angles of steel coupling beams from the second to fourth floors. Although the web plate thickness was 4mm for all steel coupling beams, the depth of steel coupling beams on the second and third floors was greater than that on the fourth and fifth floors due to the higher shear demands at the lower stores. The estimated yield rotation angle in shear was 0.0033rad for steel coupling beams at all floor levels, indicating that the steel coupling beams yielded at the early loading stage of the test corresponding to very small roof lateral drift ratio. It can be seen that the steel coupling beams on the third and fourth floors yielded earlier than that at the second floor. Since the roof lateral drift ratio exceeded 0.5%, the cracking conditions on wall piers have remained unchanged, while the shear deformation of steel coupling beams has kept increasing. Before the failure of the test model, the steel coupling beams undertook the majority of the plasticity development of the test model and consumed a considerable amount of energy through inelastic shear rotations. At the ultimate failure of the test model, the shear rotation angles of the steel coupling beam at the third and fourth floors have exceeded the limit value of 0.08 rad (AISC 361 2016).

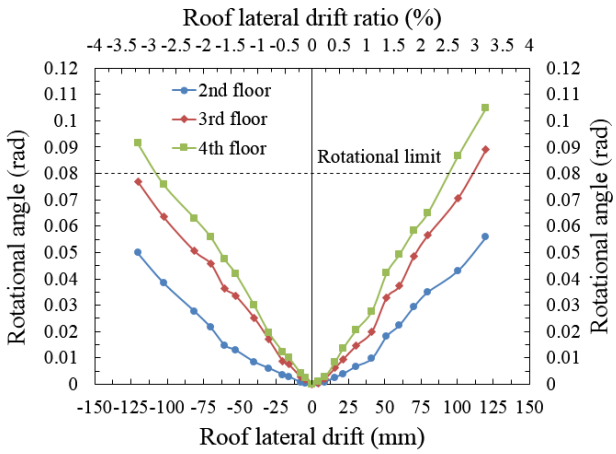

Fig. 12 Shear rotation angle of steel coupling beams

3.3 Strains at wall reinforcement and VBE of SPSW

The strain gages attached to the rebars along the bottom sections of wall piers are identified as shown in Fig. 13. Since the rebars at the exterior sides of wall piers fractured at the ultimate condition of the test, only those strains measured at characteristic loading stages are plotted in Fig. 13 corresponding to the elastic (P_e), yield (P_y), and peak load (P_m) conditions, respectively. The yield strain of rebars ε_y is also shown by red dashed lines. At the early loading stage, the strains of all rebars were small. After the test model yielded, the strains of rebars at the boundary regions of each wall pier increased significantly. However, the strains of the rebars at the exterior and interior boundary regions did not equally increase. According to Fig. 13, the strains at locations *A* and *J* exceeded the yield strain and were much larger than those at locations *E* and *F*. At the peak lateral load, the strains at the outermost rebars on the exterior sides of the two walls (i.e. locations *A* and *J*) have become much greater than the yield strain ε_y. However, the strains at the innermost rebars on the interior sides of the two walls (i.e. locations *E* and *F*) were still below the yield strain. The exterior vertical boundary element of the SPSW yielded when the roof lateral drift was about 30 mm with a corresponding roof lateral load of 550 kN.

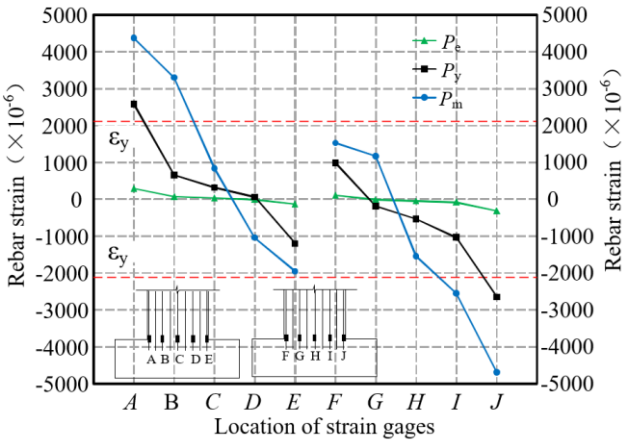

Fig. 13 Reinforcement strain variation at bottom section of wall pier

3.4 Lateral force-displacement relationship

The red solid lines in Fig. 14 are the measured lateral force versus the roof lateral drift ratio hysteretic loops of the test model. It can be seen that the hysteretic loops exhibit little pinching effect, indicating good energy dissipation behavior. The peak lateral loads were 667kN and -687kN with the corresponding roof lateral drift ratios of approximately ±1.50% in the positive and negative directions. After the peak lateral loads, the lateral load capacity of the test model didn't attenuate significantly, implying good retention capacity of the coupled SPRC wall system. The ideal lateral load carrying capacity of the test model V_{ip} was evaluated based on the measured material properties and relevant design code (JGJ138 2016). The calculated V_{ip} was also given in Fig. 14 by the dashed lines, which is very close to the measured peak lateral load capacity of the test model.

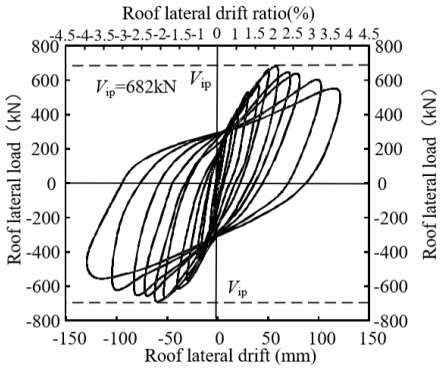

Fig. 14 Experimental roof lateral force-displacement hysteretic loops

3.5 Inter-story drift

The inter-story drift response of each story upon characteristic loading stages are plotted in Fig. 15, where P_e, P_y, P_m and P_u are corresponding to the initial concrete cracking, yielding of steel coupling beams, peak load of test model, and ultimate condition, respectively. When the initial cracking occurred, the test model deflected laterally in a flexural manner. Along with the gradual spreading of cracking from the bottom stories toward the upper stories of the wall piers, as indicated in Fig. 6, the lateral stiffness from the second to fifth stories decreased. It is obvious the coupling action provided by the steel beams caused a highly uniform distribution of cracking along the height, resulting in very similar inter-story drifts from the third to fifth stories. The plastic shear rotations of the steel coupling beams continued developing and led to a further decrease of lateral stiffness. The steel coupling beams at the third and fourth floors developed more inelastic shear rotations and caused larger inter-story drift ratios at the top three stories. At the ultimate condition, the severe spalling off of exterior boundary elements at the bottom story of wall piers and fully developed shear rotations of steel coupling beams significantly increased the inter-story drift ratios of all the stories. The fracture failure of steel coupling beams at the fourth and fifth floors made the inter-story drift even larger than the other stories.

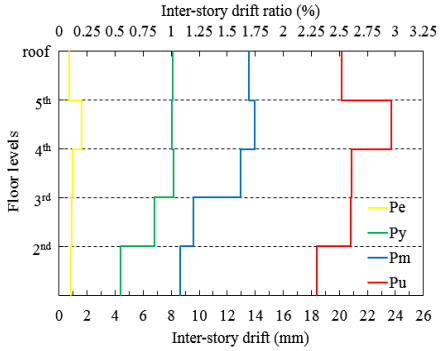

Fig.15 Inter-story drift ratios

3.6 Displacement ductility

In order to estimate the displacement ductility of the test model, the equivalent energy method was adopted (Park et al. 1988) to determine the yield displacement based on the skeleton lateral force-displacement curve (Fig. 16). As shown in Fig. 17, P_m and Δ_m are the maximum lateral force and the corresponding displacement on the skeleton curve; the ultimate condition is defined as the point on the skeleton curve where the lateral force is equal to $0.85P_m$ and the corresponding displacement Δ_u is regarded as the maximum displacement. An idealized bilinear curve consisting of an ascending segment and a flat segment corresponding to the maximum shear force P_m is developed as illustrated in Fig. 17. If the shaded regions (1) and (2), enclosed by the measured skeleton curve and the ascending segment of the idealized bilinear curve, have the same area, the displacement corresponding to the intersecting point between the ascending and flat segments of the idealized bilinear curve is taken as the yield displacement Δ_y. The lateral loads, displacements, and roof lateral drift ratios corresponding to yielding, peak lateral load and the ultimate condition of the test model are listed in Table 2. The corresponding roof lateral drift ratios δ_y, δ_m and δ_u are also provided.

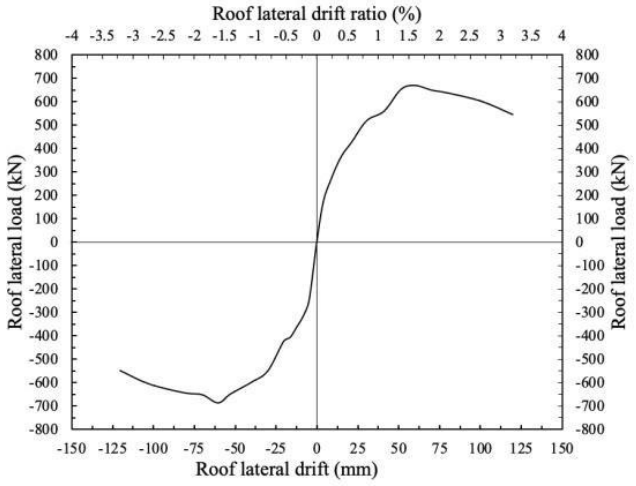

Fig. 16 Roof lateral load-displacement skeleton curve

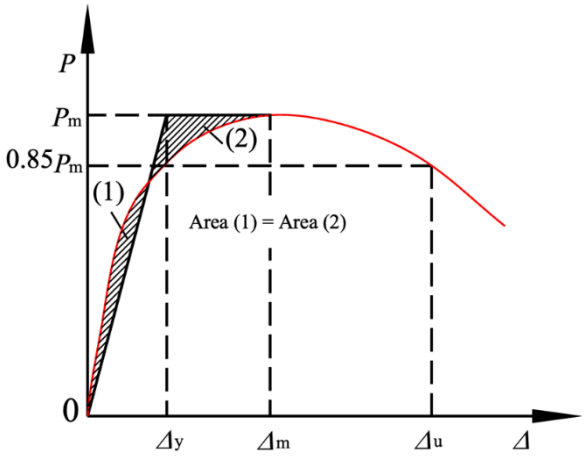

Fig. 17 Diagram of equivalent energy method

The ductility behavior of the test model was evaluated by the displacement ductility coefficient μ, which is calculated as the ratio of Δ_u to Δ_y, where Δ_y and Δ_u are the lateral displacements at yielding and the ultimate condition, respectively. The value of the ductility coefficient μ is given in Table 2. The test model had an average ductility coefficient exceeding 3.0, indicating a great post-yield deformation capacity of the coupled system

Table 2. Characteristic parameters of test model

Loading direction	Yielding			Peak load			Ultimate condition			
	P_y/kN	Δ_y/mm	δ_y	P_m/kN	Δ_m/mm	δ_m	P_u/kN	Δ_u/mm	δ_u	μ
+	541.2	36.8	1/108	667.7	60.0	1/67	567.5	111.7	1/36	3.0
-	-572.1	-34.3	1/117	-687.8	-60.4	1/66	-584.6	-109.5	1/37	3.2

3.7 Secant stiffness degradation

The secant stiffness of the test model corresponding to the peak lateral load of the first loading cycle at each displacement amplitude was used to evaluate the stiffness degradation of the test model (Fig. 18). The secant stiffness degraded with the increase of the roof lateral drift. Before the roof lateral drift ratio of 0.4%, the secant stiffness reduced abruptly due to the rapid cracking development of the wall piers; after that, the degradation rate of secant stiffness decreased with the increase of the roof lateral drift, indicating that the cracking conditions of the wall piers remained stable. During this stage, the plasticity development of the steel coupling beams contributed to the majority of the stiffness degradation of the test model.

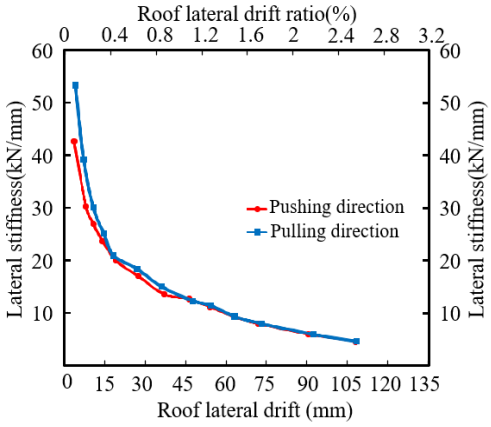

Fig. 18 Stiffness degradation

3.8 Yielding sequence of test model components

The components yielding sequence of the test model implies how a coupled SPRC wall system behaves during an earthquake event. The desirable failure mechanism can be verified by examining the yielding sequence of the test model components according to the test results. Fig. 19 shows the roof lateral displacement versus the lateral force skeleton curve of the test model, where the yielding events of various components are marked. At a very small lateral drift, the concrete at the bottom of the wall boundary region started to crack first. The concrete cracking further developed along the entire height of the wall pier due to the coupling action of the steel coupling beams (SCB) at all floor levels. Then the SCBs at the fourth and fifth floors yielded in shear, followed by the shear yielding of SCBs at the second and third floors. Once all the SCBs have yielded, the shear forces transferred from the SCBs to the wall piers no longer increased, resulting in the approximately stable cracking conditions of the wall piers. The continuous plastic rotations of the SCBs contributed most of the post-yield deformation and energy dissipation of the test model. Along with a further increase of the roof lateral displacement, the exterior vertical boundary element of the embedded SPSW yielded. And the concrete on the exterior sides of the bottom boundary regions of wall piers started to crash before the test model reached its peak lateral load capacity. After the concrete crushing and spalling off, the outermost rebars of the wall piers fractured. The load carrying capacity decreased until the ultimate failure of the test model.

4. Numerical analysis

In order to broaden the limited test results and search for an optimal design, finite element (FE) analysis was conducted for a more comprehensive coverage on the seismic behavior of the coupled SPRC wall system. Then the parametric studies using the FE modeling techniques verified against the test results were conducted to investigate the influences of key design parameters such as axial load ratio α, sectional steel plate ratio σ_s, and flexure-to-shear ratio of steel coupling beam $M_p/(V_p l_n)$ on the overall seismic performance of the coupled SPRC system. The FE analysis platform ABAQUS was used for numerical studies.

4.1 Modeling of concrete

The concrete damaged plasticity (CDP) model was used to simulate concrete behavior. It describes the irreversible damage to concrete based on a combination of uncorrelated multi-hardening plasticity and isotropic damage elasticity. Tensile cracking and compressive crushing are assumed to be the two main failure mechanisms. The evolution of the yield surface is controlled by tensile and compressive equivalent plastic strains. As shown in Fig. 19, the compressive stress-strain relationship was divided into elastic, hardening and softening stages; and the tensile stress-strain relationship was divided into elastic and softening stages. The compressive and tensile stress-strain relationships can be determined according to the Chinese code (GB50011 2010). The initial elasticity modulus E_0 can be calculated using the stress $\sigma_{c,}$ e_0 and strain $\varepsilon_{c,}$ e_0 corresponding to the elastic limit by Eq. (2). Generally, $\sigma_{c,\,e0}$ is 1/3 of f_c, where f_c is the concrete compressive strength.

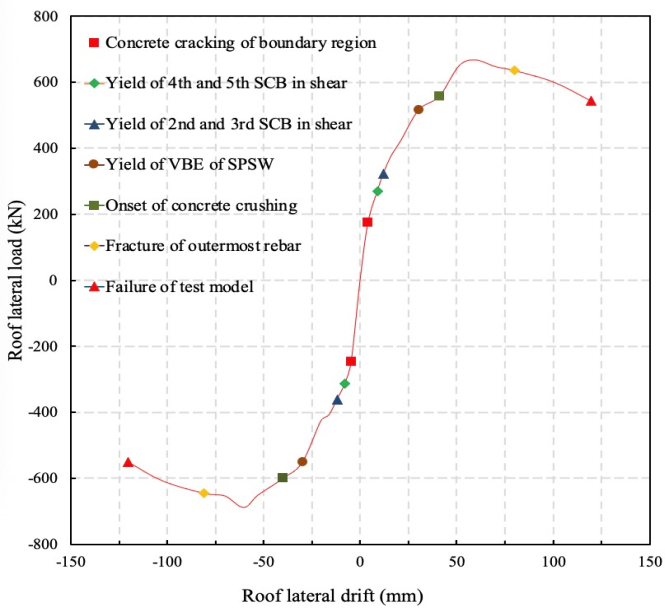

Fig. 19 Yielding sequence of test model

$$E_0 = \frac{\sigma_{c,e0}}{\varepsilon_{c,e0}} \quad (2)$$

In the CDP model, instead of stress and strain in the compression or tensile plasticity stage, stress and inelastic strain are selected. Inelastic strain is not the same as plastic strain. The cracking strain in the tensile stage, $\varepsilon t,in$, and the inelastic strain in the compression stage, $\varepsilon c,in$, can be calculated by Eqs. (3)-(4). The relationship between plastic strain and inelastic strain can be seen in Fig. 20.

$$\varepsilon_{t,in} = \varepsilon_t - \frac{\sigma_t}{E_0} \quad (3)$$

$$\varepsilon_{c,in} = \varepsilon_c - \frac{\sigma_c}{E_0} \quad (4)$$

where E0 is the initial elasticity modulus, σ_t is the stress at any point during the hardening phase of tension, and ε_t is the strain corresponding to σ_t; σ_c and ε_c are the stress and strain during the hardening phase of compression.

The concrete stiffness deteriorates due to damage. The uniaxial compressive damage variable, Dc, and the tensile damage variable, Dt, were introduced in the stress-strain relationship. The uniaxial tension and compression stress-strain relationship of concrete can be expressed by Eqs. (5)-(6). Inserting Eqs. (3)-(4) into Eqs. (5)-(6), the $D_c(D_t)$- $\varepsilon_{c,in}(\varepsilon_{t,in})$ relationship could be obtained. Then the tension plastic strain, $\varepsilon_{t,p}$ and the compression one, $\varepsilon_{c,p}$ can be calculated based on Eqs. (7)-(8).

$$\sigma_t = (1 - D_t)E_0(\varepsilon_t - \varepsilon_{t,p}) \quad (5)$$

$$\sigma_c = (1 - D_c)E_0(\varepsilon_c - \varepsilon_{c,p}) \quad (6)$$

$$\varepsilon_{t,p} = \varepsilon_{t,in} - \frac{D_t}{1-D_t}\frac{\sigma_t}{E_0} \quad (7)$$

$$\varepsilon_{c,p} = \varepsilon_{c,in} - \frac{D_c}{1-D_c}\frac{\sigma_c}{E_0} \quad (8)$$

For other input parameters in the CDP model, the dilation angle is 38°, the flow potential eccentricity is 0.1, the ratio of the second stress invariant on the tensile meridian-to-that on the compressive meridian equals 0.667, the ratio of biaxial concrete compressive strength-to-the uniaxial concrete compressive strength is 1.16, and the concrete Poisson's ratio is 0.2.

4.2 Modeling of reinforcement and SPSW

To simulate the reinforcement and the structural steel members, the stress-strain relationship considering the yield platform, steel hardening, and failure of steel is used (Eurocode 3 2005). Poisson's ratio of steel was 0.3. The stress-strain relationships of the reinforcement and steel members are given by the following expressions, in which the key parameters were obtained from the material test results.

$$\sigma = \begin{cases} \varepsilon E_s & \varepsilon \le \varepsilon_p \\ f_y & \varepsilon_p \le \varepsilon \le \varepsilon_y \\ f_y + \frac{f_u - f_y}{\varepsilon_s - \varepsilon_y}(\varepsilon - \varepsilon_y) & \varepsilon_y \le \varepsilon \le \varepsilon_s \\ f_u & \varepsilon_s \le \varepsilon \le \varepsilon_t \\ f_u\left(1 - \frac{\varepsilon - \varepsilon_t}{\varepsilon_u - \varepsilon_t}\right) & \varepsilon_t \le \varepsilon \le \varepsilon_u \\ 0 & \varepsilon > \varepsilon_u \end{cases} \quad (9)$$

where Es is the Young's modulus of steel, σ is the stress of steel, fy is the yield stress, fu is the tensile stress, εp is the proportional limit stain, εy is the yield stain, εs is the strength ultimate strain, εt is the strength degradation strain, and εu is the ultimate strain. The stress-strain relationship of the steel is given on Fig. 21.

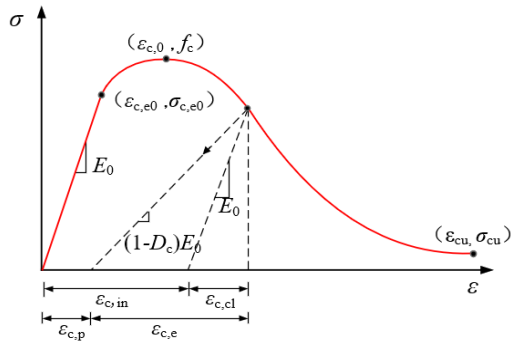

(a) compression

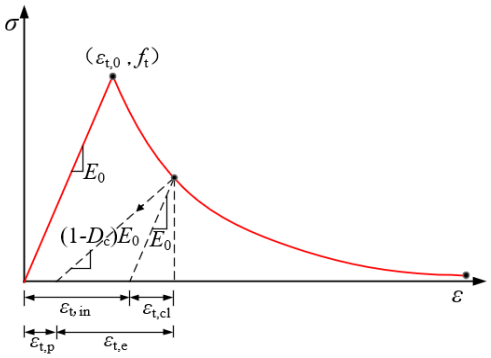

(b) tension

Fig. 20 Stress-strain curves of concrete

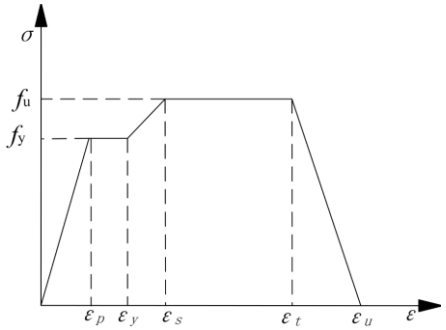

Fig. 21 Stress-strain curves of steel and reinforcement

4.3 Finite element types and meshing

The 3D 8-node solid element with reduced integration C3D8R was used to model the concrete. The SPSW components were modeled by the 4-node doubly curved shell elements with reduced integration S4R. The rebars were modeled by the 2-node linear displacement truss elements T3D2. In order to provide both accurate results and less computational cost, an average mesh size of 50 mm×25 mm×50 mm (i.e., depth × width × height) was applied to most of the concrete elements. The size of SPSW and reinforcement was approximately 50 mm (Fig. 22). Further refinement of the meshing yields negligible changes in analysis results.

4.4 Bond-slip and boundary conditions

Well-distributed studs welded to the steel plates can ensure the interaction between RC and embedded SPSW. In addition, the horizontal and vertical distributed reinforcement as well as transverse reinforcement running through the holes reserved on the SPSW at construction can further help strengthen the connection of the two different materials. As the test results showed, these configurations have joined the concrete and steel plate together well to carry the load and deform together. Thus, the steel plate, structural steel, and reinforcements are embedded into the concrete using the Embedded Constraint option in ABAQUS, assuming a perfect bond. The bottom surface of the foundation was restrained against all degrees of freedom. The side surface of the loading beam was coupled to a reference point located at its center, which is free to displace in other directions. Uniform compressive force was applied on the top surface of the loading beam, and the displacement-controlled loading history of the test was replicated and applied to the reference point.

4.5 Verification of finite element model

As shown in Fig. 23, the red dashed lines represent the simulated lateral force-displacement hysteretic loops while the black solid lines represent the experimental ones. It can be seen that the simulated and experimental lateral force-displacement loops agreed satisfactorily. In particular, the peak lateral load capacity and the post-yield strength degradation were well captured by simulation with a normalized error range from 1.86% to 4.93%. The pinching of the experimental curves was more obvious than the simulated hysteretic curves due to various factors, including but not limited to: 1) the perfect bond-slip assumption; 2) the simplified concrete damage and cracking representation, and 3) the limitations of the boundary conditions in the test setup. However, this discrepancy in pinching mainly impacts the numerical simulation of the energy dissipation capacity of the test model. The overall behavior in terms of the load carrying capacity and deformation characteristics is still simulated with satisfactory agreement with the experimental results. Fig. 24 compares the roof lateral force-displacement skeleton curves obtained by experiment and simulation. Table 3 lists the simulated and experimental lateral loads and displacements at yield, peak load, and ultimate condition. Note that the simulated displacement ductility coefficient is larger than the experimental value. The developed numerical modeling techniques can simulate the seismic performance of the coupled SPRC wall system with satisfactory accuracy.

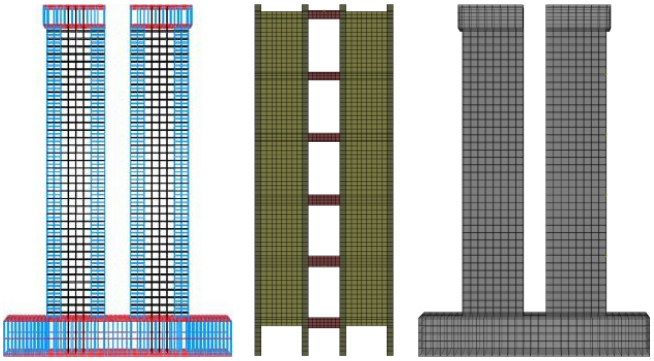

(a) reinforcement (b) SPSW (c) RC wall

Fig. 22 Meshing of FE model

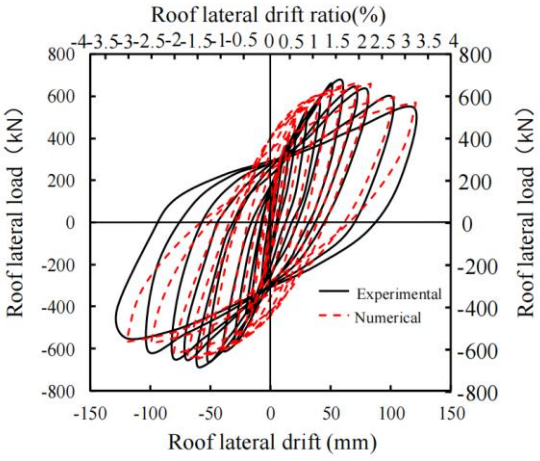

Fig. 23 Lateral load-displacement hysteretic curve

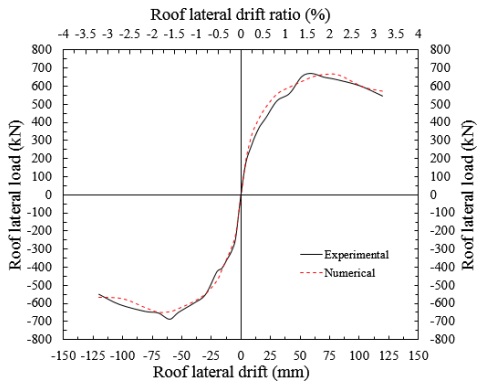

Fig. 24 Lateral load-displacement skeleton curve

Table 3. Comparison of simulated and experimental results

	Loading direction	Yield		Peak		Failure		Disp. ductility
		P_y(kN)	Δ_y(mm)	P_m(kN)	Δ_m(mm)	P_u(kN)	Δ_u(mm)	
Experiment	(+)	541.43	36.82	667.73	60.01	567.57	111.66	3.11
	(-)	-598.89	-34.28	-687.83	-60.36	-584.66	-109.51	
Simulated	(+)	562.1	31.6	666.6	73.4	570.3	121.0	3.80
	(-)	-548.8	-30.4	-649.2	-70.0	-567.0	-120.3	

5. Parametric Studies

Adopting the verified finite element (FE) modeling techniques, extended FE models were established to further investigate the influences of key parameters on the seismic performance of coupled SPRC wall systems. The parameters considered in the parametric analyses included the nominal axial load ratio α, steel plate ratio ρ_s, and flexure-to-shear ratio of steel coupling beams $M_p/(V_p l_n)$. Five cases were assigned to each parameter to cover its value range in practical design, as summarized in Table 4.

Table 4. Parametric analyses cases

Axial load ratio, α		Steel plate ratio, ρ_s		Ratio of flexure to shear, $M_p/V_p l_n$)	
Case ID	Value	Case ID	Value (%)	Case ID	Value
A-1	0.05	B-1	3.9	C-1	2.0
A-2	0.10	B-2	5.3	C-2	1.0
A-3	0.15	B-3	6.6	C-3	0.67
A-4	0.20	B-4	8.0	C-4	0.5
A-5	0.25	B-5	9.4	C-5	0.4

5.1 Effect of axial load ratio α

In order to examine the effect of the axial load ratio, a series of analyses were carried out with the nominal axial load ratio α varying from 0.05 to 0.25 while the steel plate ratio ρ_s and the flexure-to-shear ratio of steel coupling beams remained constant at 6.6% and 1.0, respectively. This range of nominal axial load ratio between 0.05 and 0.25 is corresponding to the range of design axial load ratio below about 0.5, or moderate design axial load ratios. Fig. 25 shows the lateral force-displacement skeleton curves corresponding to different values of the axial load ratio. Table 5 summarizes the analyses results of the lateral loads and displacements corresponding to yielding, peak lateral load and ultimate condition under different axial load ratio cases. The displacement ductility coefficients are also listed. It can be seen from Fig. 25 that all of the numerical cases exhibited very close initial secant stiffness, indicating the axial load ratio had an insignificant impact on the elastic behavior. Before reaching the peak lateral load capacity, the load-displacement curves of all cases are very similar. When the axial load ratio increases, the peak lateral load capacity also improves. Beyond the peak load point, the load-displacement curves of the cases showed deviation. According to Table 5, the displacement ductility coefficient increases with the axial load ratio from 0.05 to 0.15. However, a further increase of α from 0.15 to 0.25 leads to the reduction of the ductility coefficients, implying that a moderate axial load ratio is beneficial to the ductility behavior of the coupled SPRC wall system. In the design of coupled SPRC wall systems with a high demand of ductility behavior and moderate levels of axial loads, steel plate ratio and flexure-to-shear ratio, it is best to select around 0.15 as the wall axial load ratio.

5.2 Effect of steel plate ratio ρ_s

The axial load ratio α and the flexure-to-shear ratio of the steel coupling beam $M_p/(V_p l_n)$ are fixed at values of 0.1 and 1.0, respectively; the steel plate ratio ρ_s varies from 3.9% to 9.4%. Fig. 26 exhibits the influence of the steel plate ratio ρ_s on the lateral force-displacement skeleton curves of the coupled SPRC wall system. Table 6 summarizes the numerical results of the loads and displacements corresponding to the yield, peak lateral load, and ultimate condition under different steel plate ratios. The displacement ductility coefficients are also listed. It is obvious that the steel plate ratio has a significant impact on the post-yield behavior of the coupled system. Along with the increase of the steel plate ratio, the peak lateral load capacity also increases. However, after the peak lateral load is exceeded, the lateral load capacity decreases faster with increasing steel plate ratio. The displacement ductility coefficient increases when the steel plate ratio increases from 3.9% to 6.6% and then decreases with the further increase from 6.6% to 9.4%. In the design of coupled SPRC wall systems with a high demand of ductility behavior and moderate levels of axial loads and flexure-to-shear ratio, it is best to select around 6.6% as the wall steel plate ratio.

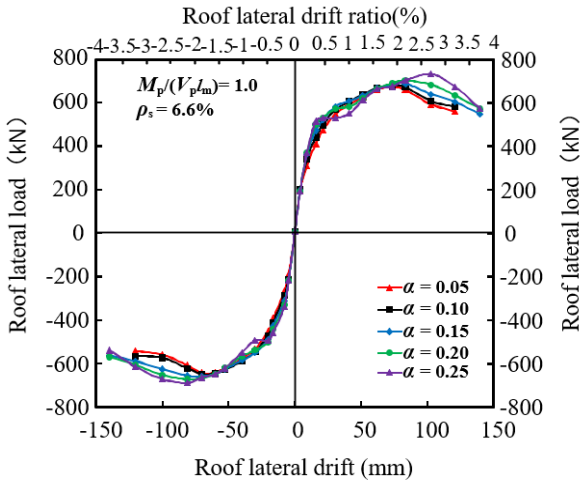

Fig. 25 Influence of α on lateral load-roof drift ratio skeleton curves

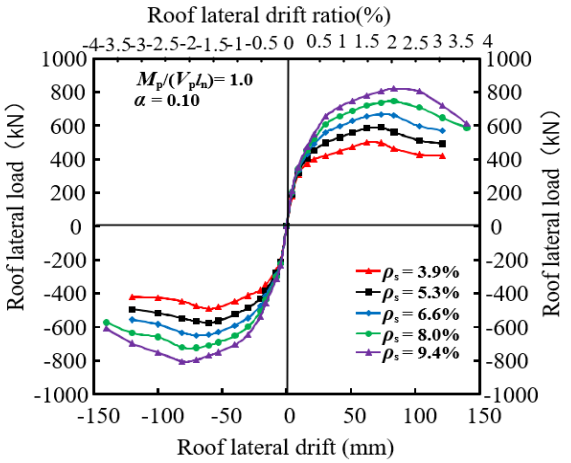

Fig. 26 Influence of ρ_s on lateral load-roof drift ratio skeleton curves

5.3 Effect of flexure-to-shear ratio of steel coupling beam $M_p/(V_p l_n)$

In these cases, the steel plate ratio ρ_s and the axial load ratio α are fixed at the values of 6.6% and 0.1, respectively; the flexure- to-shear ratio of steel coupling beam $M_p/(V_p l_n)$ varies from 0.4 to 2.0. According to AISC 341 (AISC 341 2016), within the analyses cases when $M_p/(V_p l_n)$ is equal to 0.4 or 0.5, inelastic responses of steel coupling beams involve the combination of shear and flexural yielding, while shear yielding will dominate the inelastic response when $M_p/(V_p l_n)$ is equal to 0.667, 1.0 or 2.0. Fig. 27 shows the influence of $M_p/(V_p l_n)$ on the roof lateral drift-lateral load skeleton curves of the coupled SPRC walls. Table 7 summarizes the numerical results of the loads and displacements corresponding to the yield, peak and ultimate states under different $M_p/(V_p l_n)$ values. The displacement ductility coefficients are also listed. With larger $M_p/(V_p l_n)$, the peak lateral load is smaller. The coupled SPRC wall system achieves the largest displacement ductility coefficient when $M_p/(V_p l_n)$ is 1.0 corresponding to shear yielding domination of steel coupling beam behavior. The numerical cases with steel coupling beams dominated by the combination of flexural and shear yielding exhibited less ductile than those with steel coupling beams dominated by shear yielding. In the design of coupled SPRC wall systems with a high demand of ductility behavior and moderate levels of axial loads, steel plate ratio, it is best to select about 1.0 as the flexure-to-shear ratios of the steel coupling beams.

Table 5. Parametric analyses results for various α (ρ_s=6.6%, $M_p/(V_p l_n)$=1)

	Loading direction	Yield		Peak		Failure		Disp. ductility coefficient
		Py(kN)	△y(mm)	Pm(kN)	△m(mm)	Pu(kN)	△u(mm)	
A-1	(+)	552	34.2	661	73.4	562	114	3.37
	(-)	-544	-32.1	-644	-70.0	-547	-110	
A-2	(+)	562	31.6	667	73.4	570	121	3.82
	(-)	-549	-30.4	-649	-70.0	-567	-120.3	
A-3	(+)	574	31.7	676	83.5	574	127	4.29
	(-)	-554	-30.6	-658	-70	-559	-140	
A-4	(+)	566	35.3	690	83.5	587	132	3.98
	(-)	-549	-33.3	-673	-81	-572	-139	
A-5	(+)	554	43.6	720	103	612	130	3.18
	(-)	-538	-37.8	-690	-81	-586	-127	

Table 6. Parametric analysis results for various ρ_s (α=0.10, $M_p/(V_p l_n)$=1.0)

	Loading direction	Yield		Peak load		Failure		Disp. ductility coefficient
		Py(kN)	△y(mm)	Pm(kN)	△m(mm)	Pu(kN)	△u(mm)	
-1	(+)	412	26.5	498	62	423	90.4	3.17
	(-)	-403	-27.1	-491	-60.4	-418	-79	
B-2	(+)	490	29.2	589	73.4	500	99.5	3.37
	(-)	-481	-29	-577	-60.4	-490	-96.7	
B-3	(+)	562	31.6	667	73.4	570	121	3.82
	(-)	-549	-30.4	-649	-70.0	-567	-120.3	
B-4	(+)	628	34.9	745	83.5	633	126.1	3.75
	(-)	-614	-32.9	-724	-70	-615	-127.8	
B-5	(+)	693	36.8	821	83.5	697	132	3.54
	(-)	-684	-36.4	-805	-81	-684	-127	

Table 7. Parametric analysis results for various Mp/(Vpln) (ρ_s =6.6%, α=0.10)

	Loading direction	Yield		Peak load		Failure		Disp. ductility coefficient
		Py(kN)	△y(mm)	Pm(kN)	△m(mm)	Pu(kN)	△u(mm)	
C-1	(+)	529	39	634	83.5	539	121	3.16
	(-)	-514	-37.4	-615	-81.1	-523	-120	
C-2	(+)	562	31.6	667	73.4	570	121	3.82
	(-)	-549	-30.4	-649	-70.0	-567	-120.3	
C-3	(+)	599	31	726	62	618	107	3.43
	(-)	-598	-30.9	-720	-60.4	-612	-106	
C-4	(+)	631	30.7	770	62	654	97	2.85
	(-)	-642	-33	-784	-60.4	-667	-84.1	
C-5	(+)	666	32.9	824	62	700	91.8	2.62
	(-)	-670	-33	-818	-60.4	-696	-81	

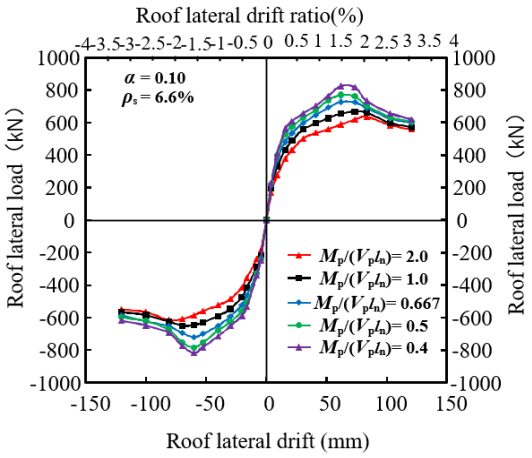

Fig. 27 Influence of $M_p/(V_p l_n)$ on lateral load-roof drift ratio skeleton curves

6. Conclusions

In this research program, experimental and numerical parametric investigations were conducted on the coupled SPRC wall system. The 1/4-scaled five-story and two-pier coupled SPRC wall test model was loaded with failure to study the cyclic responses such as failure pattern, hysteretic loops, skeleton curves, stiffness and strength degradation characteristics, energy dissipation capacity and coupling beam shear deformation. An additional fifteen numerical models were built and analyzed to better the understanding on the influences of key design parameters on the overall behavior of the coupled SPRC wall system. The following conclusions can be drawn.

- The plasticity development and failure pattern observed during the test indicated that the steel coupling beams can fulfill the expected coupling action for the coupled wall system. At the early loading stage, the concrete cracking was initiated at the bottom region of the wall pier and then extended along the entire wall height, showing a relatively uniform damage distribution pattern. When the steel coupling beams started to yield, the wall pier cracking condition remained stable. The plasticity development was concentrated on the steel coupling beams with significant shear rotations up to 0.1 radian. After the failure of steel coupling beams due to excessive shear deformation, the exterior side of the wall pier boundary region developed concrete crushing and spalling off, ultimately leading to the fracture of longitudinal rebars or buckling of vertical boundary element of the SPSW.
- The experimental results showed the coupled SPRC walls can be designed to have great lateral strength, post-yield deformation and energy dissipation capacities as well as strength retention capacity. The ultimate displacement ductility coefficient can reach 3.0 and the roof lateral drift angle can reach 1/36. It is noted that the exterior side of the bottom boundary region of the wall pier suffered much more severe damage than its interior counterpart.
- The finite element numerical modeling techniques can be used to simulate the overall behavior of the coupled SPRC wall system in terms of peak lateral load capacity, post-yield behavior, and back-bone characteristics with satisfactory accuracy and efficiency.
- The parametric analyses results demonstrate that increasing the axial load ratio and steel plate ratio or decreasing the flexure-to-shear ratio of the steel coupling beam can enhance the lateral load carrying capacity of the coupled SPRC wall system. With respect to the displacement ductility behavior, however, a medium value of 0.15 for the axial load ratio or 6.6% for the steel plate ratio can result in the best displacement ductility coefficient. Steel coupling beams with a shear-to-flexure ratio of 1.0 can lead to the best displacement ductility behavior, where the plastic behavior is dominated by shear yielding.
- This research successfully proves that the coupling action can be developed in SPRC wall piers joined by steel coupling beams. The coupled SPRC walls can be designed to have adequate displacement

ductility coefficients up to about 4.0. The results of this study can provide both experimental and numerical background for current seismic design codes to recognize the coupled SPRC wall system to design the core tubes of super tall buildings with improved material efficiency and seismic performance.

- Due to the limitations of the laboratory facility, the reported experimental results can only be used to validate the numerical simulation of coupled SPRC walls subjected to moderate levels of design axial load ratios. The behavior of the coupled SPRC walls under high axial load ratios may be significantly different from that under moderate axial load ratios. Future research is needed to investigate the influence of high axial load ratios on the seismic performance of the coupled SPRC walls.

Acknowledgments

This research project is financially sponsored by the Natural National Science Foundation of China (Grant No. 51978101) when the corresponding author was previously affiliated with Chongqing University. The authors would like to express their sincere thanks and appreciation to the supporting agency of this project.

References

AISC 361-16. Seismic provisions for structural steel buildings. Chicago: American Institute of Steel Construction; 2016.

ACI 318-19. Building code requirements for structural concrete (ACI 318-19) and commentary (ACI 318R-19). Farmington Hills: American Concrete Institute; 2014.

Abdelatee AE,Kent AH. Design of coupled wall structures as evolving structural systems. Eng Struct. 2014; 73: 100-113. https://doi.org/10.1016/j.engstruct.2014.05.002

ASCE 7-16. Minimum design loads for buildings and other structures. Chicago: American Society of Civil Engineers; 2016.

Bengar HA and Aski RM. Performance based evaluation of RC coupled shear wall system with steel coupling beam. Steel Compos Struct. 2016; 20 (2): 337-55; https://doi.org/10.12989/scs.2016.20.2.337

Broberg M, Shafaei S, Kizilarslan E, Seo J, Varma AH, Bruneau M and Klemencic R. Capacity design of coupled composite plate shear wall-concrete-filled system. J Struct Eng. 2022; 148(4): 04022022; https://doi.org/10.1061/(ASCE)ST.1943-541X.0003296

Borello DJ, Fahnestock LA. Behavior and mechanisms of steel plate shear walls with coupling. J Constr Steel Res. 2012; 74: 8-16; https://doi.org/10.1016/j.jcsr.2011.12.009

Cheng MY, Fikri R, Chen CC. Experimental study of reinforced concrete and hybrid coupled shear wall systems. Eng Struct. 2015; 82: 214- 25; https://doi.org/10.1016/j.engstruct.2014.10.039

Zhang B, Wu YT, Zhaou Q, Bai JL, Yang YB. Energy-balance based plastic design and analysis of hybrid coupled wall system. Structures, 2021, 33: 4096-4111. https://doi.org/10.1016/j.istruc.2021.07.017

Dey S and Bhowmick AK. Seismic performance of composite plate shear walls. Structures. 2016; 6: 59-72; https://doi.org/10.1016/j.istruc.2016.01.006

Das R et al. Characterization and optimization of a steel beam to RC wall connection for use in innovative hybrid coupled wall systems. Struct. 2020; 23: 111-25; https://doi.org/10.1016/j.istruc.2019.10.011

El-Tawil S, Harries KA, Fortney PJ, Shahrooz BM and Kurama Y. Seismic design of hybrid coupled wall systems: state of the art. J Struct Eng. 2010; 136 (7): 755-69; https://doi.org/10.1061/(ASCE)ST.1943-541X.0000186.

EN 1993-1-1. Eurocode 3: Design of steel structures-Part 1-1: General rules and rules for buildings. Brussels: European Committee for Standardization; 2005.

FEMA 461. Interim Testing Protocols for Determining the Seismic Performance Characteristics of Structural and Non-structural Components. Washington: Applied Technology Council; 2007.

Gorji MS and Cheng JJ. Plastic analysis and performance-based design of coupled steel plate shear walls. Eng Struct. 2018; 166: 472-84; https://doi.org/10.1016/j.engstruct.2018.03.048

GB 50011-2010. Code for Seismic Design of Buildings. Beijing: Ministry of Housing and Urban-rural Development; 2010. (in Chinese)

GB/T 228.1. Metallic materials-tensile testing-Part 1: Method of test at room temperature. Beijing: Ministry of Housing and Urban-rural Development; 2010. (in Chinese)

GB/T 50081. Standard for test methods of concrete physical and mechanical properties. Beijing: Ministry of Housing and Urban-rural Development; 2019. (in Chinese)

JGJ 138-2016. Code for design of composite structures. Beijing: Ministry of Housing and Urban-rural Development; 2016. (in Chinese)

Kizilarslan E, Bruneau M. Verification of seismic response modification factors of uncoupled composite plate shear walls/concrete filled. J Strut Eng. 2023; 04023060; 10.1061/JSENDH.STENG-11783. https://doi.org/10.1061/JSENDH.STENG-11783

Kizilarslan E, Broberg M, Shafaei S, Varma AH, Bruneau M. Seismic design coefficients and factors for coupled composite plate shear walls/concrete filled (CC-PSW/CF). Eng Struct. 2021; 244: 112766; https://doi.org/10.1016/j.engstruct.2021.112766

Nguyen NH and Whittaker AS. Numerical modeling of steel-plate concrete composite shear walls. Eng Struct. 2017; 150: 1-11; https://doi.org/10.1016/j.engstruct.2017.06.030

Oh K, Ha H, Jo B and Lee K. An analytical study on structural performance evaluation of coupled steel plate shear wall systems. Int J Steel Struct. 2019; 19(1): 1-13; https://doi.org/10.1007/s13296-018-0082-2.

Park R. Ductility evaluation from laboratory and analytical testing. Proceedings of the 9th World Conference on Earthquake Engineering. 1988; Tokyo-Kyoto.

Shafaei S, Varma AH, Seo J, Klemencic R. Cyclic Lateral Loading Behavior of Composite Plate Shear Walls/Concrete Filled. J Strut Eng. 2021; 04021145; https://doi.org/10.1061/(ASCE)ST.1943-541X.0003091

Varma AH, Shafaei S, Klemencic R. Steel modules of composite plate shear walls: Behavior, stability, and design. Thin Walled Struct. 2019; 145: 106384.
https://doi.org/10.1016/j.tws.2019.106384

Wang B, Jiang H and Lu X. Seismic performance of steel plate reinforced concrete shear wall and its application in China Mainland. J Constr Steel Res. 2017; 131: 132-143; https://doi.org/10.1016/j.jcsr.2017.01.003

Wang W, Ren YZ, Lu Z, et al. Experimental study of the hysteretic behavior of corrugated steel plate shear walls and steel plate reinforced concrete composite shear walls. J Constr Steel Res. 2019; 160: 136-152; https://doi.org/10.1016/j.jcsr.2019.05.019

Zhang B, Wu YT, Zhou Q, et al. Energy-balance based plastic design and analysis of hybrid coupled wall system. Struct. 2021; 33: 4096-4111; https://doi.org/10.1016/j.istruc.2021.07.017

Disclaimer